



## Powered Low-Speed Experimental Aerodynamic Investigation of an Over-Wing-Mounted Nacelle Configuration

Downloaded from: <https://research.chalmers.se>, 2024-04-10 22:39 UTC

Citation for the original published paper (version of record):

Silva, V., Lundbladh, A., Xisto, C. et al (2023). Powered Low-Speed Experimental Aerodynamic Investigation of an Over-Wing-Mounted Nacelle Configuration. Journal of Aircraft, In Press. <http://dx.doi.org/10.2514/1.C037653>

N.B. When citing this work, cite the original published paper.

# Powered Low-speed Experimental Aerodynamic Investigation of an Over-wing Mounted Nacelle Configuration

Vinicius T. Silva \*

*GKN Aerospace, 461 81 Trollhättan, Sweden.  
Chalmers University of Technology, 412 58 Gothenburg, Sweden*

Anders Lundbladh †

*GKN Aerospace, 461 81 Trollhättan, Sweden.*

Carlos Xisto‡, Petter Miltén§, and Isak Jonsson¶

*Chalmers University of Technology, 412 58 Gothenburg, Sweden*

Over-wing integration of ultra-high bypass turbofan engines can be a solution for next-generation commercial transport aircraft, since it eliminates the ground clearance issue, and it has the potential to reduce ground noise due to acoustic shielding. Moreover, a unique characteristic of this installation type is the powered lift benefit at low-speed flight conditions. This paper aims to experimentally investigate the effect of the engine power setting on the low-speed aerodynamic performance of an over-wing mounted nacelle configuration comprising a conventional tube-and-wing layout. Thus, low-speed wind tunnel tests were performed for a half-span powered scale model of the aforementioned configuration. The effect of the engine power setting on the wing lift and spanwise pressure distributions was investigated. The experiments were carried out for angles-of-attack varying from  $0^\circ$  to  $6^\circ$  and inlet mass flow ratios up to 2.4. The results were used to validate computational fluid dynamics simulations conducted for the same wind tunnel conditions. It has been shown that a significant powered lift benefit can be achieved for the studied configuration, without a penalty in the net propulsive force, and that the lift increases linearly with the inlet mass flow ratio. Furthermore, it was observed that the engine power setting largely influences the pressure distributions along the wing, especially at the spanwise sections closer to the nacelle. The low momentum zone created upstream of the engine at high power settings reduces the pressure at the wing's upper surface, which is the main factor responsible for the increased lift. By taking advantage of such behavior, drag can potentially be reduced at takeoff and climb due to a lower flap setting required for the same lift.

## I. Nomenclature

### Symbols

$A_0$	=	Captured area
$A_{hi}$	=	Highlight area
$AoA$	=	Angle of attack
$C_l$	=	Lift coefficient
$C_p$	=	Pressure coefficient
$C_q$	=	Discharge coefficient
$\dot{m}$	=	Mass flow
$F_{net}$	=	Net propulsive force
$F'_x$	=	Axial force (parallel to the balance)

---

\*Research Engineer, Future Concepts, GKN Aerospace, Flygmotorvägen 1, 461 81 Trollhättan, Sweden; [vinicius.tavaressilva@gknaerospace.com](mailto:vinicius.tavaressilva@gknaerospace.com)

†Technical Fellow, Future Concepts, GKN Aerospace, Flygmotorvägen 1, 461 81 Trollhättan, Sweden.

‡Associate Professor, Mechanics and Maritime Sciences, Chalmers University of Technology, Hörsalsvägen 7A, 412 58 Gothenburg, Sweden.

§PhD Candidate, Mechanics and Maritime Sciences, Chalmers University of Technology, Hörsalsvägen 7A, 412 58 Gothenburg, Sweden.

¶Researcher, Mechanics and Maritime Sciences, Chalmers University of Technology, Hörsalsvägen 7A, 412 58 Gothenburg, Sweden.

$F'_z$	=	Normal force (perpendicular to the balance)
$L$	=	Lift
$M_\infty$	=	Freestream Mach number
MFR	=	Mass flow ratio
$p$	=	Static pressure
$p_t$	=	Total pressure
$q_\infty$	=	Freestream dynamic pressure
$Re$	=	Reynolds number
$Re_c$	=	Chord-based Reynolds number
$S_{ref}$	=	Reference area
$T_t$	=	Total temperature
$x_i$	=	Individual error sources
$\delta_{xi}$	=	Error of the independent variables
$\epsilon_\varsigma$	=	Total uncertainty
$\eta$	=	Normalized wing spanwise section
$\rho_\infty$	=	Freestream density
$\varsigma$	=	Dependable function

## Acronyms

BPR	=	Bypass ratio
CRM	=	Common research model
EDF	=	Electric ducted fan
ESC	=	Electronic speed controller
HWB	=	Hybrid wing body
MAC	=	Mean aerodynamic chord
OWN	=	Over-wing nacelle
PWM	=	Pulse Width Modulation
UHBPR	=	Ultra-high bypass ratio
UWN	=	Under-wing nacelle

## II. Introduction

To attain higher propulsive efficiency and lower specific fuel consumption, the next-generation turbofan engines for civil aircraft will feature considerably higher bypass ratios (BPRs) and lower fan pressure ratios (FPRs) than those of the state-of-the-art engines, and, consequently, larger engines and nacelles. The integration of engines referred to as ultra-high bypass ratio (UHBPR) turbofans will likely pose a major challenge to the aeronautical industry, owing to strict ground clearance constraints necessary for a safe aircraft operation. The conventional under-wing nacelle (UWN) installation might lead to prohibitively longer and heavier landing gears, and, therefore, the aircraft manufacturers might be forced to search for unconventional integration options. Over-wing nacelle (OWN) integration is a potential solution to this issue since it eliminates the ground clearance problem. Additionally, such installation choice provides the potential for ground noise reduction due to the acoustic shielding effect [1–3]. Other potential benefits of OWN installations are reduced intake distortion and powered lift at low-speed flight conditions [4].

There are certain drawbacks associated with OWN installations, including increased noise levels perceived by the passengers due to the proximity of the engines to the cabin. In the case of aft-mounted over-wing engines, the center of gravity shifts rearward, requiring that the entire fuselage is moved forward relative to the wing [5]. This shortens the tail moment arm, requiring larger vertical and horizontal tails and resulting in increased tail drag and weight. Additionally, over-wing mounted engines are more difficult to reach for maintenance, resulting in slower operations and higher costs.

Over-wing nacelle integration has acquired a bad reputation in the past since this type of installation would normally be outperformed by conventional UWN cases [6], due to high-pressure disturbances at the wing's upper surface during cruise. Nonetheless, with the development of the design, optimization, and computational fluid dynamics (CFD) methods, there is some evidence that OWN integration can be an aerodynamically feasible option. Several recent

studies have investigated over-wing installation of UHBPR engines [7–12]. A work by Hooker et al. [12] is of particular interest. They conducted shape optimizations for different wing configurations, nacelle locations, and BPRs. They found that the solution with the highest fuel burn reduction potential was an OWN configuration, featuring a trailing edge mounted engine and a low wing, which had an improvement of 5% in aerodynamic efficiency compared to a conventional UWN configuration. Silva et al. [8] have shown that, by employing a coupled wing-reshaping and engine position optimization study, the aerodynamic performance of OWN installations can be improved significantly. A common finding of the aforementioned studies was that mounting the engines above the wing and near its trailing edge has a major impact on the aircraft’s lift and drag since the flow field around the wing’s upper surface is substantially affected by the upstream momentum variation imposed by the engine. At cruise speeds, this effect is detrimental to lift and drag, because the external diffusion in the captured streamtube induces a pressure rise at the upper surface of the wing. On the contrary, during low-speed flight conditions, at high engine power settings, the flow accelerates towards the intake, creating a low-pressure zone on the upper surface of the wing, which results in a powered lift benefit, as shown in the study carried out by Wick et al. [4]. They conducted powered tests at the Lockheed Martin Low-speed Wind Tunnel to investigate the aerodynamic performance and stability of the Hybrid Wing Body (HWB), an innovative airlifter configuration featuring over-wing nacelles mounted near the wing’s trailing edge [13]. One of their conclusions was that the lift could be increased without a thrust or drag penalty. The powered lift effect is well known and has been thoroughly investigated in the past for OWN and UWN installations, [14–16], for cases where the exhaust jet is blown on the flaps, and deflected downward by the Coanda effect. However, the lift benefit of a trailing edge mounted engine has not yet been broadly explored.

Other experimental studies highlight the potential benefits and drawbacks of over-wing mounted engines. Chan et al. [17] have carried out unpowered transonic tests to validate the aerodynamic performance of the HWB and efficiency benefits of the OWN installation as compared to the traditional under-wing installation. Robes and Catalano [18] have conducted tests for an unpowered over-wing nacelle configuration in comparison to a clean wing configuration and observed that the over-wing nacelle mount was able to delay turbulent separation and increase lift at high angle of attack, AoA. Moreover, de Vires et al. [19] have conducted an experimental investigation of an over-wing mounted propeller interaction with the wing’s boundary layer, and concluded that there is a clear potential to increase lift, although such benefit is largely dependant on the system design.

The powered lift effect is evident for the HWB configuration, and there are clear indications in the literature that over-wing installations might improve low-speed aircraft performance. However, it is not clear that the powered lift benefit would be as pronounced for a conventional tube-and-wing airframe, with over-wing mounted engines, as it has been found to be for the HWB configuration. Therefore, to further investigate this phenomenon, an experimental campaign was conducted in the Chalmers Low-Speed Wind Tunnel for a half-span, 5.3% scale, powered model of an OWN configuration with a conventional tube-and-wing airframe. The major results and findings of the tests are reported in this paper. The results were used to verify the powered lift benefit for this configuration in particular and to validate Reynolds-averaged Navier-Stokes (RANS) CFD simulations.

### III. Engine Power Setting Effect

Similarity with real flight operating conditions cannot be achieved in the Chalmers low-speed wind tunnel, which operates at the low Reynolds number,  $Re$ , and incompressible flow regimes. Even though freestream Mach numbers,  $M_\infty$ , up to 0.18 can be achieved, which can be representative of takeoff speeds, local compressible effects, such as high-incidence supersonic accelerations inside the nacelle, cannot be reproduced. Nevertheless, this paper aims to capture the impact of the momentum variation upstream of the engine, for an OWN configuration, on the wing lift and pressure distributions, which depends mainly on the engine power setting. A non-dimensional parameter that characterizes the engine power setting is the intake mass flow ratio (MFR), defined as follows:

$$\text{MFR} = \frac{A_0}{A_{hi}} = \frac{\dot{m}_0}{\rho_\infty V_\infty A_{hi}} \quad (1)$$

where  $A_0$  is streamtube captured area and  $A_{hi}$  is the inlet highlight area. For a typical cruise condition, the MFR is lower than unity, meaning that the flow experiences diffusion upstream of the intake and spills around the nacelle lip. For low-speed flight conditions, such as takeoff and climb, there is no spillage, and the MFR is higher than unity, which leads to flow acceleration toward the intake. It is expected that, compared to a conventional under-wing installation at the same AoA, over-wing mounted engines will experience a loss in lift for a cruise condition ( $\text{MFR} < 1$ ), due to the external diffusion in the captured streamtube, and that there will be a lift benefit for the low-speed conditions ( $\text{MFR} > 1$ ),



referred to as powered lift, owing to a low-pressure region created in the vicinity of the engine. This is a phenomenon that can be observed both in low turbulence wind tunnels and in real flight conditions depending majorly on the MFR, and therefore it will be the focus of this study. Figure 1 illustrates the impact of the MFR on the pressure field upstream of the engine for the same AoA. It is clear that the engine power setting has a major impact on the flowfield upstream of the nacelle. Figure 1 shows that when  $MFR < 1$  a high-pressure zone is formed ahead of the nacelle, and Fig. 1b shows the opposite behavior for an MFR higher than unity.

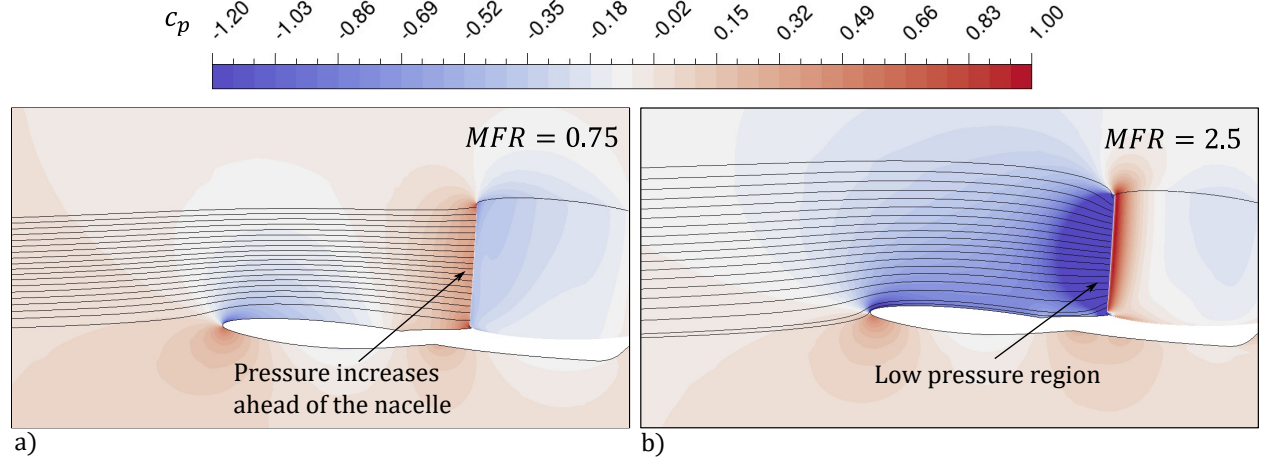


**Fig. 1** Effect of inlet MFR on the pressure field upstream of the engine for a)  $MFR=0.75$  and b)  $MFR=2.5$ .

#### IV. Airframe and nacelle geometries

The integrated over-wing nacelle geometry used to create the test model was designed using the methodology presented in [7, 8], where the aerodynamic investigation of an OWN configuration was carried out. The chosen airframe geometry was the wing-body NASA Common Research Model (CRM) [20, 21], which was scaled to the size of an A320, based on its mean aerodynamic chord (MAC). The model features an axisymmetric nacelle with an ultra-short inlet, designed as part of the work conducted in [22], which presented a multipoint design method for ultrashort-nacelles. The pylon shape was created by vertically overlapping symmetric NACA four-digit airfoils. The OWN geometry was scaled based on the size of the available electric ducted fan (EDF) to create the 5.3% scale powered, as described in section V.A.

#### V. Experimental Setup and Methodology

The experiments presented in this paper were carried out in the L2 wind tunnel at the Chalmers Laboratory of Fluids and Thermal Sciences. The L2 tunnel is a closed, low turbulence tunnel with a maximum freestream velocity,  $V_\infty$ , of 60 m/s. The test section has a cross-section of 1.8 m  $\times$  1.2 m and 3.0 m long. Figure 2 shows the OWN model mounted in the wind tunnel. All the test cases were conducted at  $V_\infty = 20$  m/s, with a chord Reynolds number,  $Re_c$ , of  $3.05 \times 10^5$ , with respect to the model's MAC.

##### A. Over-wing Nacelle Scale Model

The assembled half-span 5.3% scale model and its main components are depicted in Fig. 3. Figure 3a provides an overview and description of all components. The supporting structures, such as the wing, pylon, and main fuselage, are made out of aluminum 6061. The model was powered by a Schuebeler DS-82-DIA HST, a 5.3 kW EDF with a 120 mm fan shroud diameter. The EDF, enclosed by a short nacelle, is shown in Fig. 3b. It was controlled by an MGM TMM 40063-3 electronic speed controller (ESC). The nacelle is attached to the wing through a hollow pylon where the power cables to the motor and pneumatic pipes to the nacelle are routed. The wing test section, pressure channels, and connectors are shown in Fig. 3c. The test section was 3D printed using Stereolithography (SLA), allowing for easy integration of internal pressure channels. Pneumatic pipes are connected to the wing test section by Scanivalve RC2/040-10 (GLD) connectors. Figure 4 shows the model's front and side views and general dimensions. It has a

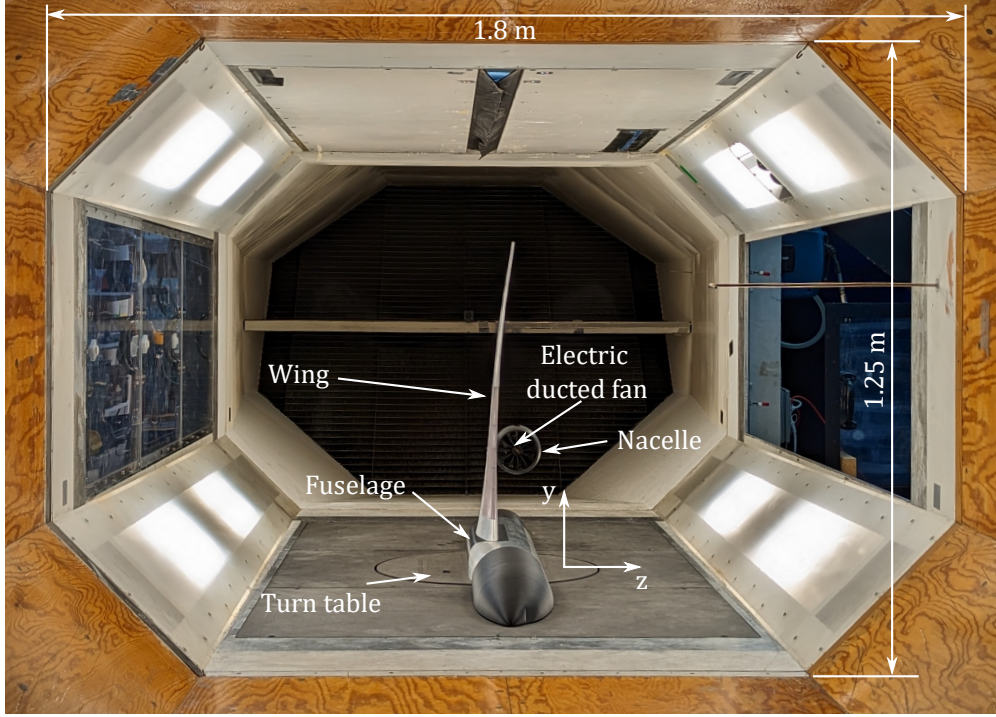


**Fig. 2 Over-wing nacelle model mounted in the wind tunnel (front view).**

semi-span of 930 mm, a fuselage length of 1983 mm, and a nacelle maximum diameter and length of 141 mm and 182 mm, respectively.

## B. Instrumentation

The model was mounted in the Chalmers L2 wind tunnel on a turn table and manually aligned to the flow with an estimated accuracy of  $\pm 0.5^\circ$ . The wind tunnel freestream velocity, density, and temperature are provided by a FCO-510 micromanometer. The tunnel freestream velocity is matched to a Prantl-tube inserted upstream of the test section. The temperature is measured by an RTD-100 sensor. All the sensor values in the described test campaign are gathered simultaneously with data from the micromanometer through the commercial software LabView.

### 1. Pressure Taps

The wing test section was instrumented with 66 pressure taps, distributed along four spanwise sections of constant vertical coordinates, inboard and outboard of the nacelle, at the following positions:  $y = 228.3$  mm ( $\eta = 0.246$ ),  $y = 282.5$  mm ( $\eta = 0.304$ ),  $y = 333.4$  mm ( $\eta = 0.359$ ),  $y = 394.9$  mm ( $\eta = 0.425$ ), where  $\eta$  is the spanwise position normalized by the wing semi-span. The location of the pressure taps is shown in Fig. 4. The static pressure data were acquired using a PSI-9116 pressure scanner with a sampling rate of 1 kHz and averaged over 4 seconds. Two scanivalves with 48 port revolvers each were utilized to sweep over the pressure taps on the wing test section.

### 2. Force Balance

A specially made six-axis 196-6H RUAG balance was utilized to measure the lift,  $L$ , and the net propulsive force,  $F_{net}$  acting on the wing. Figure 4 shows a detail of the balance mounting. The balance data were sampled with a 1 kHz frequency and averaged over 5 seconds using an SCXI-1314T terminal block to an SCXI-1520 strain/bridge input module. Since the balance rotates with the model, the measured forces were projected onto the wind tunnel coordinate system to obtain  $L$  and  $F_{net}$ , as shown in Eqs. 2 and 3, respectively.

$$L = F'_x \sin(\text{AoA}) + F'_z \cos(\text{AoA}) \quad (2)$$

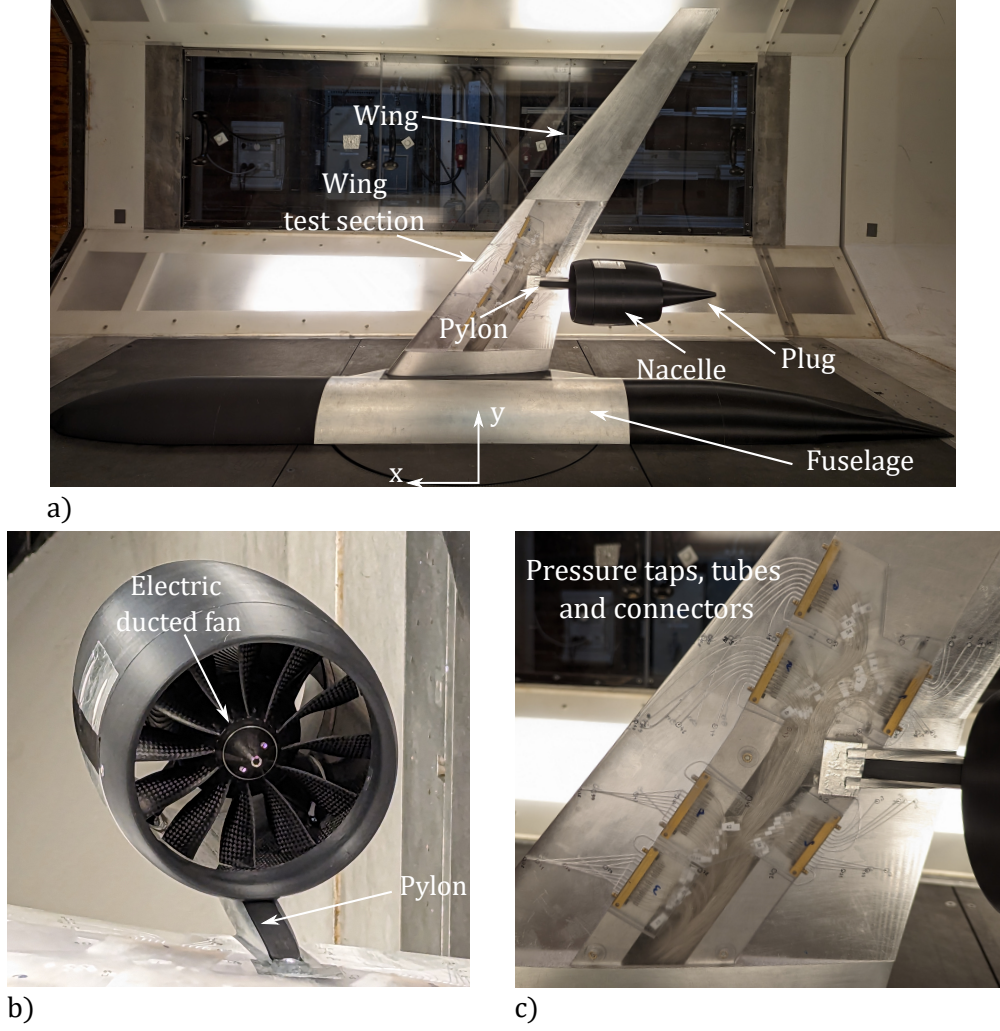


**Fig. 3 Over-wing nacelle model: a) side view and main components; b) detail of the electric ducted fan enclosed by the nacelle and attached to the wing through a pylon; c) close-up of the test section, showing pressure taps, tubes, and connectors.**

$$F_{net} = F'_x \cos(\text{AoA}) - F'_z \sin(\text{AoA}) \quad (3)$$

where  $F'_x$  and  $F'_z$  are the axial and normal forces, measured in the parallel and perpendicular directions to the balance's horizontal axis, respectively. The lift coefficient,  $C_l$ , is defined as follows:

$$C_l = \frac{L}{q_\infty S_{ref}} \quad (4)$$

where  $q_\infty$  is the freestream dynamic pressure, given by  $p_{t,\infty} - p_\infty$ , and  $S_{ref}$  is the reference area of the scale model.

### 3. Mass Flow Ratio

The engine MFR was obtained by two pressure taps placed inside the nacelle's inlet. They were placed at circumferential positions  $85^\circ$  inboard and  $85^\circ$  outboard of the pylon. The total pressure loss for short intakes at low-speed freestream conditions is expected to be very small, and thus the total pressure at the fan face  $p_{t,2}$  was estimated by assuming a constant intake pressure recovery,  $\pi$ , of 0.9995, where  $\pi = p_{t,2}/p_{t,\infty}$ . With the average static pressure from the taps,  $p_2$ , and the estimated fan face total pressure,  $p_{t,2}$ , the Mach number at the fan face,  $M_2$ , can be calculated by

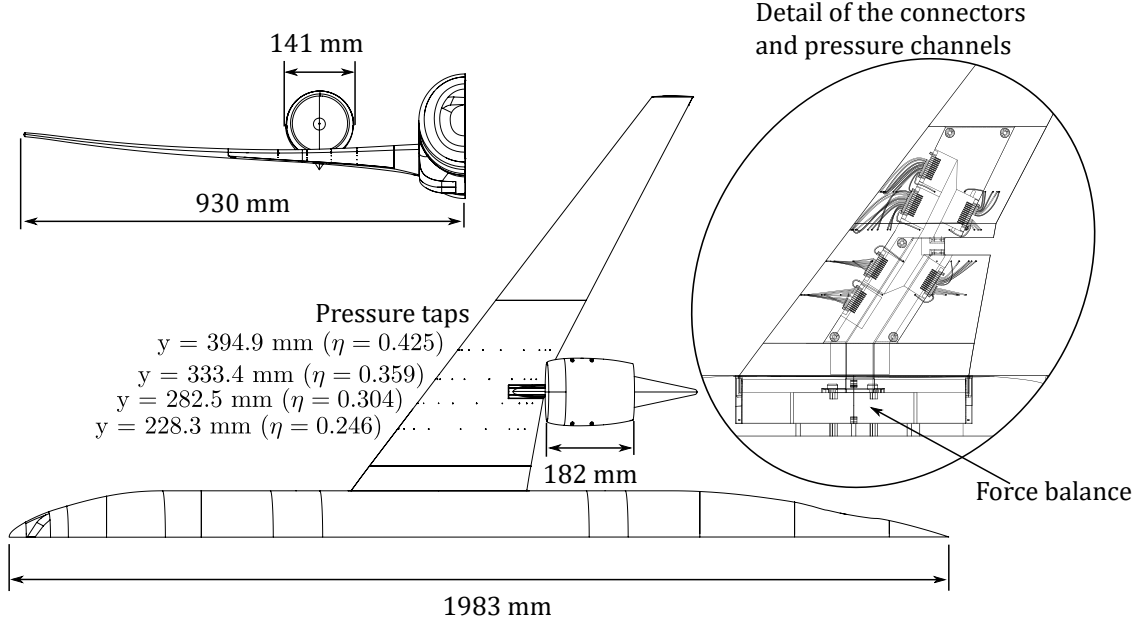


**Fig. 4 Over-wing nacelle model's main dimensions, pressure taps' locations, and detail of the connectors and force balance.**

assuming a uniform flow and isentropic relations for an ideal gas, and by extension, the mass-flow through the fan,  $\dot{m}_0$ , can be calculated as follows:

$$\dot{m}_0 = C_q \frac{A_2 p_{t,2}}{\sqrt{T_{t,2}}} \sqrt{\frac{\gamma}{R}} M_2 \left( 1 + \frac{\gamma - 1}{2} M_2^2 \right)^{-\frac{\gamma+1}{2(\gamma-1)}} \quad (5)$$

where  $C_q$  is a discharge coefficient. Finally, the intake MFR can be calculated by Eq. 1. The derivation of  $C_q$  is described later in section V.C.

#### 4. Other Sensors

The fan rotational speed was measured by a hall sensor (HASS 200-S) on one of the motor power cables. The ESC temperature was monitored by using a K-type thermocouple. The EDF was controlled from LabView by generating a pulse width modulation (PWM) signal using a NI-6210 data acquisition (DAQ) device.

### C. Uncertainty Assessment

The Talyor expansion method, as shown in Eq. (6), is utilized to calculate the final uncertainty,  $\epsilon_\varsigma$ , of the results presented later in this paper. Each individual error source is assumed to be normally distributed with the uncertainty of  $\delta_{x_i}$  as typical in standards such as ISO 17025 [23] or ASME PTC 19.1 [24].

$$\epsilon_\varsigma(x_1, x_2, \dots, x_n) = \left\{ \sum_{i=1}^n \left( \frac{\partial \varsigma}{\partial x_i} \cdot \delta_{x_i} \right)^2 \right\}^{1/2} \quad (6)$$

Where  $\varsigma$  is the dependable function and  $x_i$  are the independent variables of the expression. The uncertainty assessment of each individual variable is described as follows. The upper limit of the error in the monitoring equipment of the wind in the tunnel is  $\pm 0.1$  m/s,  $\pm 0.1^\circ\text{C}$ , and  $\pm 0.25\%$  of absolute pressure. None of them provide a substantial contribution to the final uncertainty. The balance was calibrated by the manufacturer down to  $0.1\%$  fsd (full-scale deflection) which agrees well with four in-situ control points performed before and after the model was mounted in the tunnel. Any interference from cables or pressure pipes contact was not gathered in these in-situ control points. Based on an in-house calibration with an FCO-560 calibrator, the PSI-9116 pressure scanner uncertainty can be described by  $0.15\% \pm 0.6$  Pa, [25]. A sampling time of 5 seconds and a sampling frequency of 500 Hz make any substantial statistical error unlikely.



The pressure taps had a settling time of 500 milliseconds between each revolver step, which is within the time response for a 0.8 mm inner diameter, 3 m pipe, and a pressure difference of 200 Pa. Effects from pressure tap hole imperfections have been assessed for similar geometries operating at similar conditions and manufactured using the same machine, showing a negligible effect [26]. The mechanical resolution of the mounting table is  $0.05^\circ$  with a mounting bias of  $\pm 0.75^\circ$  from lack of suitable mechanical reference. Therefore, a bias alignment between the numerical and experimental results up to  $\pm 0.75^\circ$  should be expected.

As mentioned in section V.B.3, a discharge coefficient,  $C_q$  is necessary for the MFR measurements; however, no assessment of  $C_q$  was feasible within the current test campaign. Therefore, a numerical discharge coefficient was derived to match the  $F_{net}$  obtained numerically and experimentally. A  $C_q = 0.9$  was utilized for all the data presented later in this work.

## VI. Numerical Methodology

The data from the experiments were compared to CFD simulations for the same freestream conditions and set up as the wind tunnel. The wind tunnel walls were included in the computational domain to account for blockage effects. Hybrid meshes were generated by using the commercial software Pointwise. The surface meshes, generated using the quad-dominant algorithm, comprise triangles and quadrilaterals. For the near-wall elements, the T-Rex algorithm was used to create anisotropic hexahedral, tetrahedral, prism, and pyramid elements, whilst isotropic hexahedral layers with tetrahedral transitions populated the rest of the computational domain, by employing the Voxel algorithm [27]. The computational domain is defined between the half-span aircraft geometry and the wind tunnel's walls. The height of the wall-adjacent cells was set so that  $y^+ < 1$ , in order to resolve the viscous sub-layer. A total of four grids, with sizes varying from  $79.9 \times 10^6$  to  $85.8 \times 10^6$  cells, were generated in this study for AoAs of  $0^\circ$ ,  $2^\circ$ ,  $4^\circ$ ,  $6^\circ$ . Figure 3 shows the surface and volume meshes for AoA =  $6^\circ$ .

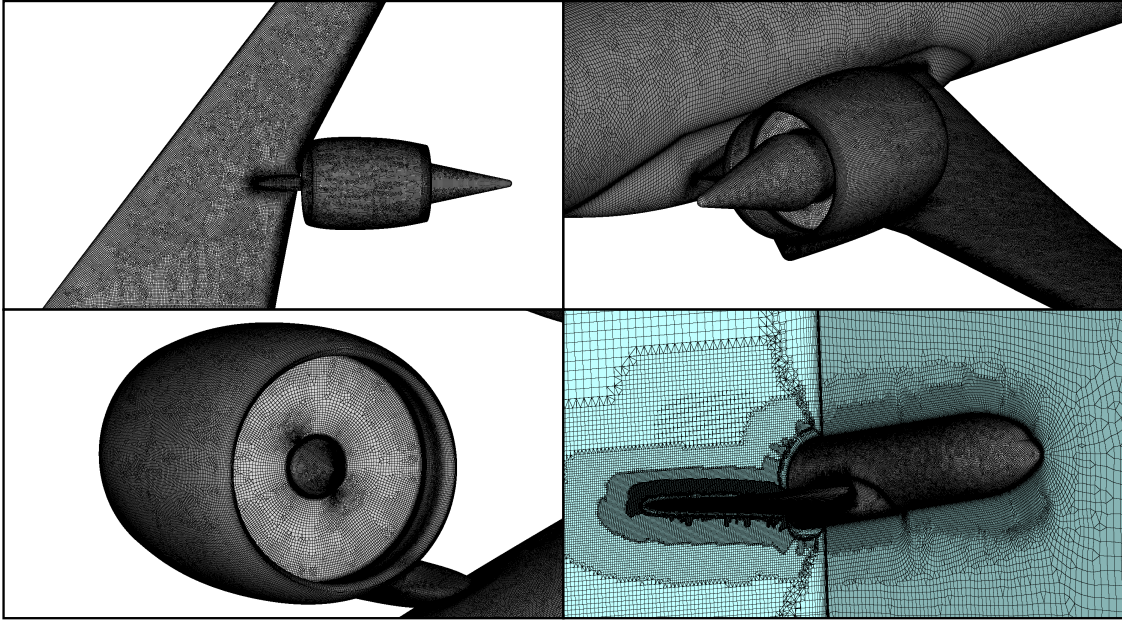


**Fig. 5 Surface and volume hybrid meshes used for the CFD simulations for AoA =  $6^\circ$ .**

The Reynolds-Averaged Navier-Stokes equations (RANS) equations were resolved by using the commercial CFD solver Ansys Fluent. The pressure-based solver was selected along with the pressure-velocity coupled algorithm. The four-equation model transition SST ( $\gamma - Re_\theta$ ) was used for turbulence closure, in order to predict laminar-to-turbulent transitions in the boundary layer. The spatial discretization of the energy and momentum equations was carried out by employing a second-order upwind scheme, whereas the flow field gradients were computed by using a least-squares cell-based method.

Figure 6 shows a schematic representation of the computational domain and boundary conditions (BC) for the CFD simulations. A pressure outlet BC is selected at the fan face, where the static pressure is specified. At the fan exit, a

mass flow inlet boundary condition is selected, where mass flow and total temperature are specified, and a target is set to the fan face mass flow so that continuity throughout the fan is obtained. At the inlet domain, a total pressure BC is selected, where total pressure, total temperature, and flow direction were the inputs, and at the outlet domain, a pressure outlet boundary condition was chosen, where the static pressure was specified.

A perfect match between the CFD and experimental inlet and outlet conditions for the fan is difficult to obtain because the fan's characteristics are unknown. In order to compare the numerical and experimental results, a static pressure sweep has been performed at the fan face in the CFD simulations. The CFD and experimental comparison was carried out for the obtained results with the closest MFR.

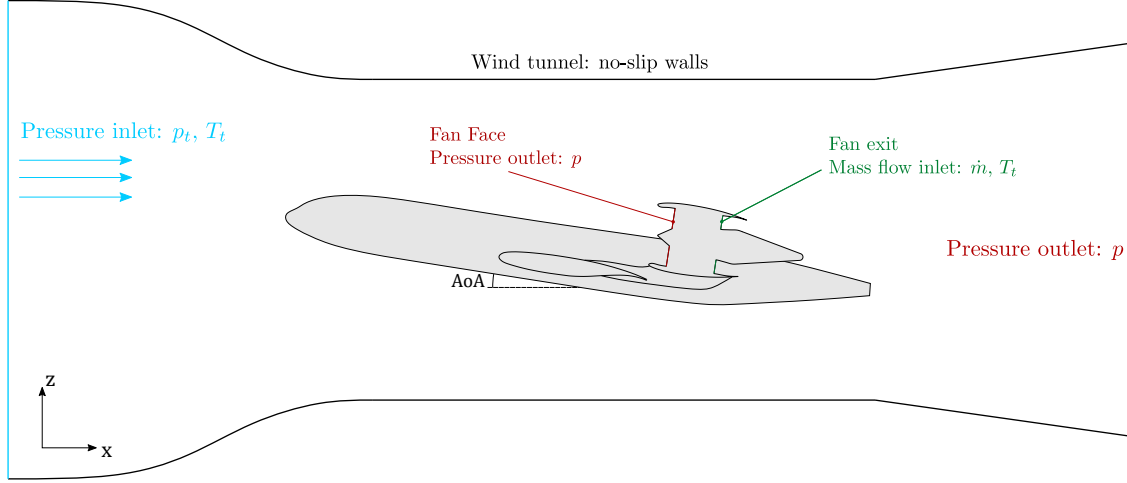


**Fig. 6 Schematic representation of the computational domain and boundary conditions.**

## VII. Results

This section presents the results obtained in the low-speed experimental campaign compared to the data from the CFD simulations. The uncertainty of the measured data is discussed in section V.C. Firstly, the impact of the engine power setting on the wing lift will be discussed. Lastly, the power setting effect on the wing pressure distributions will be addressed.

### A. The Powered Setting Effect on the Lift

The  $F_{net}$  results for different MFRs are shown in Fig. 7 for the experimental and numerical studies. The uncertainty is represented by the shaded area. For better readability, only the largest observed uncertainty is presented, for  $AoA = 2^\circ$ . A good agreement is observed between the CFD and measured data. Unsurprisingly,  $F_{net}$  increases with MFR, since the thrust should rise when the model is powered up. The impact of the  $AoA$  on  $F_{net}$  is overall small; however, the trend is that  $F_{net}$  will drop with the increased  $AoA$ , for a constant MFR, because the wing and nacelle will present more drag for higher  $AoAs$ .

The engine power setting effect on  $C_l$  is shown in Fig. 8. An overall good agreement between the numerical and measured data can be observed. A linear increase of  $C_l$  with MFR is shown, and a substantial lift augmentation can be achieved for high MFRs. This is the experimental confirmation, supported by CFD computations, that a significant powered lift benefit can be attained for a tube-and-wing aircraft, with over-wing mounted engines, at low-speed operating conditions. Compared to the unpowered cases, an average  $\Delta C_l = 0.118$  was observed for  $MFR \approx 2$ . No drag or thrust penalty was observed as the engine power setting increased. By taking advantage of this unique characteristic of OWN installations, the takeoff drag can potentially be reduced since a reduced flap setting would be required.

### B. The Power Setting Effect on the Pressure Distributions

The experimental and CFD data for  $AoA = 0^\circ$ ,  $AoA = 2^\circ$ ,  $AoA = 4^\circ$  and  $AoA = 6^\circ$  are depicted in Fig. 9, Fig. 10, Fig. 11, Fig. 12, respectively. A good overall agreement between experiments and CFD was achieved. It can be seen

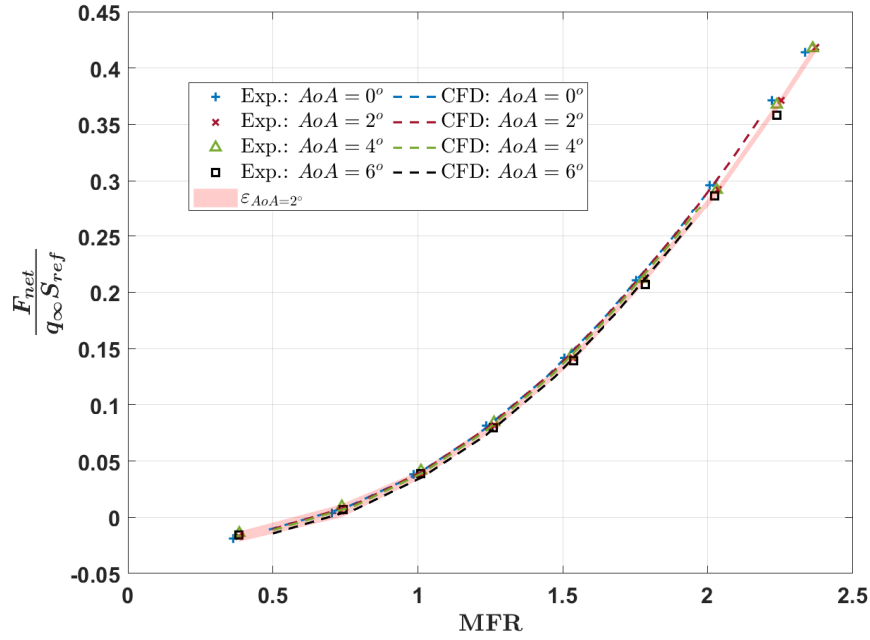


**Fig. 7** The effect of the engine MFR on the aircraft  $F_{net}$ . Experimental results compared to CFD data. The uncertainty of the measurements is represented by the shaded area. For better readability, only the largest observed uncertainty is presented, for  $AoA = 2^\circ$ .

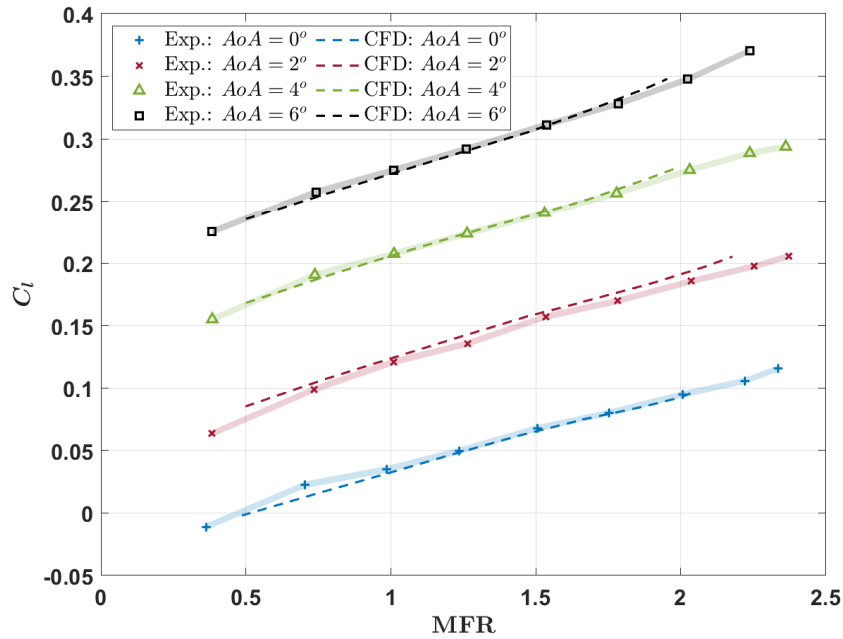


**Fig. 8** The effect of the engine MFR on the aircraft  $C_l$ . The experimental results are compared to CFD data. The uncertainty of the measurements is represented by the shaded areas.

that the selected numerical approach properly captured the low and high-pressure peaks near the wing's leading edge, as

well the pressure distributions along the pressure and suction side of the wing for different MFRs. The most visible mismatches occur near the wing's trailing edge, at the suction side, for  $\text{AoA} = 0^\circ$ ,  $\text{AoA} = 2^\circ$  and  $\text{AoA} = 4^\circ$ , and MFRs of approximately 2, especially at the spanwise position located just outboard of the pylon ( $\eta = 0.359$ ). For  $\text{AoA} = 0^\circ$ , such a mismatch is also expressive at the inboard section  $\eta = 0.304$  and for MFRs of about 1.5.

For all the high MFR cases, a complex interaction between the captured streamtube and the wing was observed from the numerical data: in the vicinity of the pylon, downstream of the captured streamtube, in the flow channel formed between the nacelle and wing's upper surface, a recirculation zone is formed, which propagates slightly downstream of the trailing edge. This is a phenomenon comprised of complex vortices and likely to be unsteady, which is not expected to be accurately predicted by RANS equations. This is the main reason for the mismatch between the experiments and CFD results.

A similar pattern is observed for all the studied AoAs: as the MFR is increased, the pressure is reduced at the wing's suction side. Such pressure reduction is the main cause for the powered lift benefit discussed in section VII.A. It can be explained by a local streamwise acceleration upstream of the nacelle, caused by the converging streamlines in the captured streamtube, a typical phenomenon that happens for  $\text{MFR} > 1$ . Unsurprisingly, the most affected spanwise sections are the ones closer to the nacelle ( $\eta = 0.304$  and  $\eta = 0.359$ ). Nevertheless, the pressure is substantially lowered for all the four locations studied in this work. Additionally, at the pressure side, an overall increase in pressure can be seen as the MFR rises. Although this will partially contribute to the powered lift benefit, it has a secondary importance when compared to the acceleration imposed by the fan to the wing's suction side.

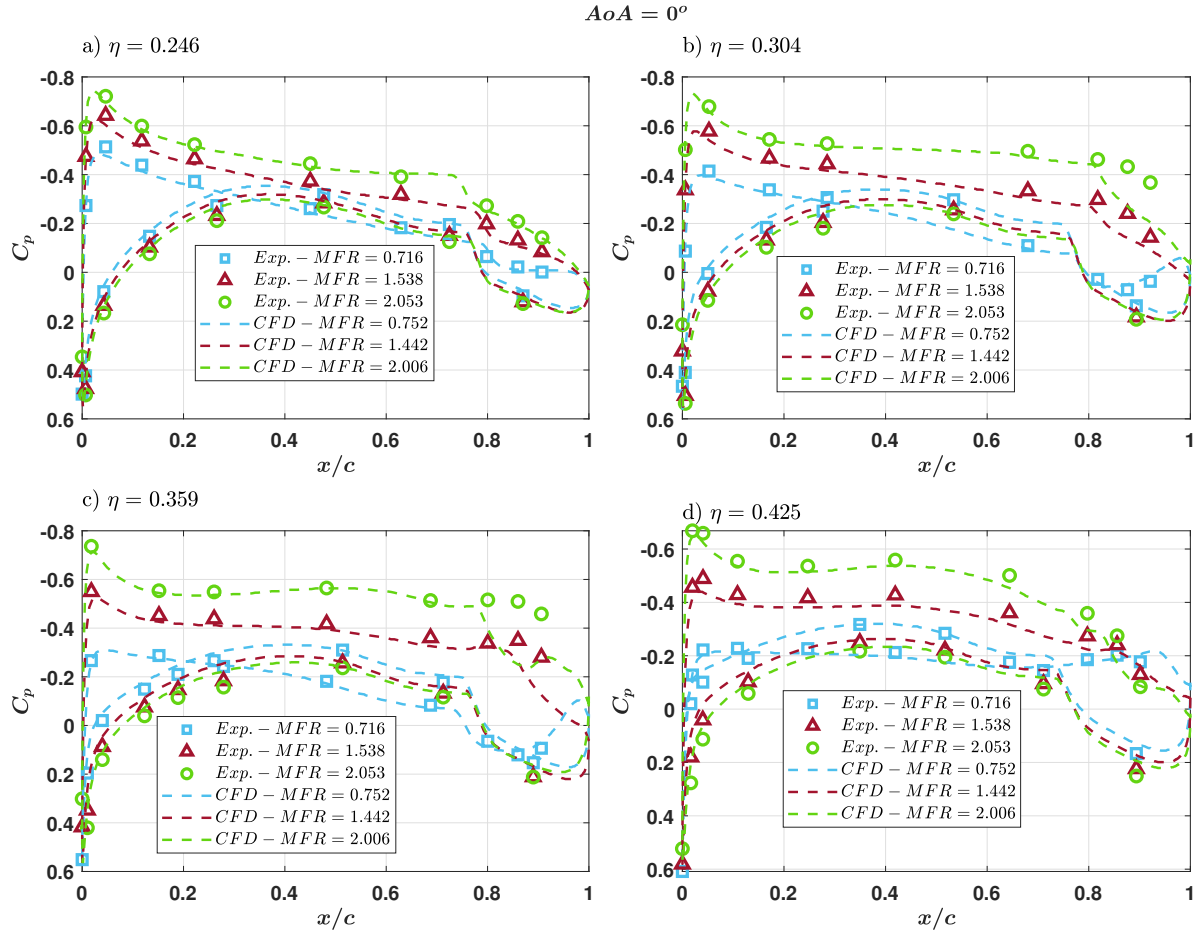


**Fig. 9** Pressure distributions for  $\text{AoA} = 0^\circ$ . The experimental results are compared with CFD data for similar MFRs.



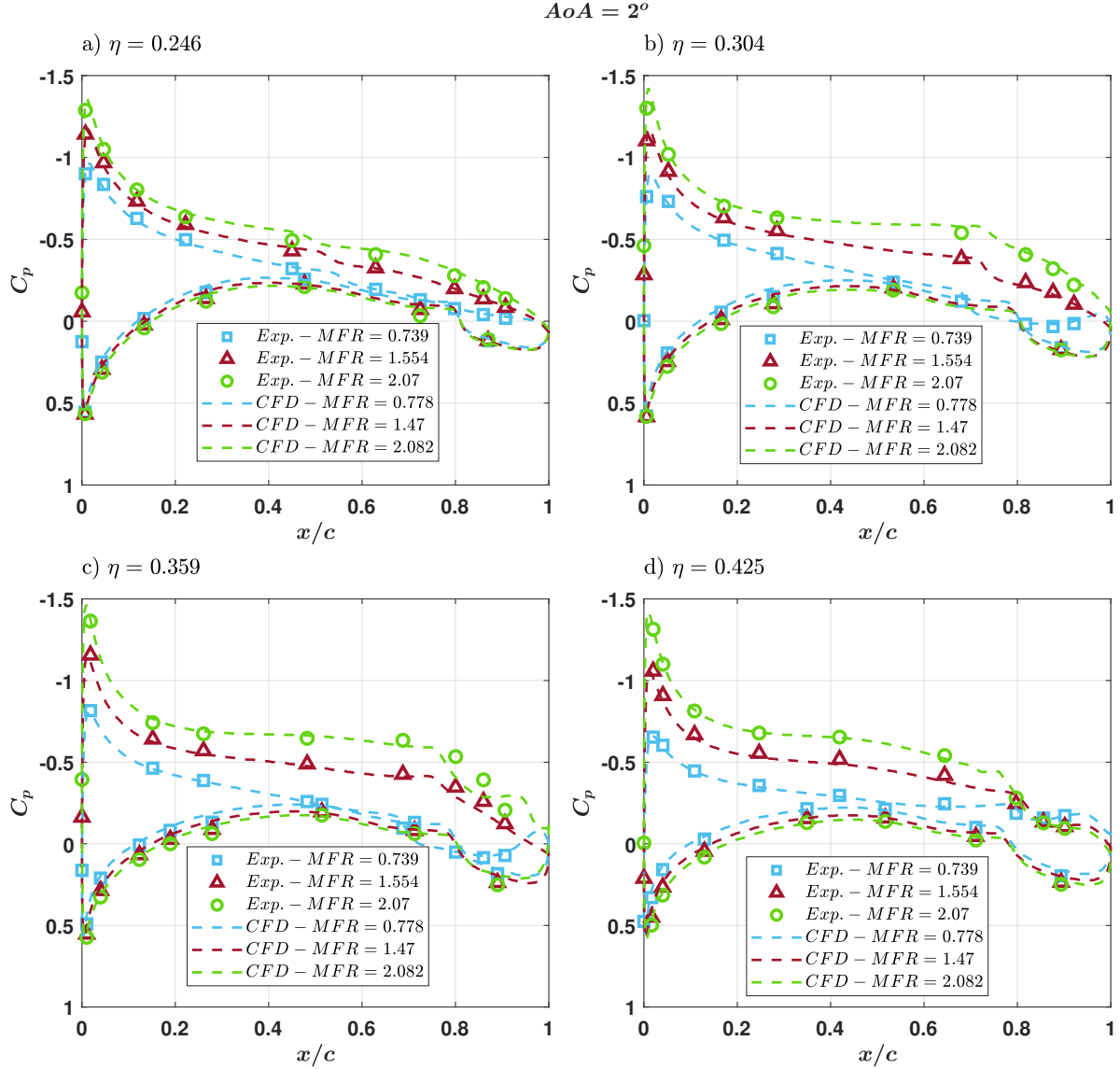


**Fig. 10** Pressure distributions for  $AoA = 2^\circ$ . The experimental results are compared with CFD data for similar MFRs.

### VIII. Conclusion

This paper presented the major results from low-speed wind tunnel tests, conducted at Chalmers University of Technology, for a powered 5.3% scale model of an OWN configuration. The main goals of the experimental campaign were to investigate the effect of the engine power setting on the lift produced by the wing and on its pressure distributions. Static pressure measurements were conducted at four different wing spanwise sections, inboard and outboard of the pylon. Moreover,  $C_l$  and  $F_{net}$  were measured by means of a six-component force balance mounted at the wing root. The test results were compared with data from RANS CFD simulations. The main findings obtained from the tests and simulations are highlighted as follows:

- It has been demonstrated numerically and experimentally that  $C_l$  increases linearly with the MFR for the studied OWN configuration at low-speed operating conditions. By taking advantage of such behavior, takeoff drag can potentially be reduced, since lower flap settings would be required.
- For  $MFR > 1$ , the streamwise converging streamlines in the captured streamtube cause an acceleration upstream of the nacelle, which is responsible for substantially reducing the pressure at the wing's suction side, and thus

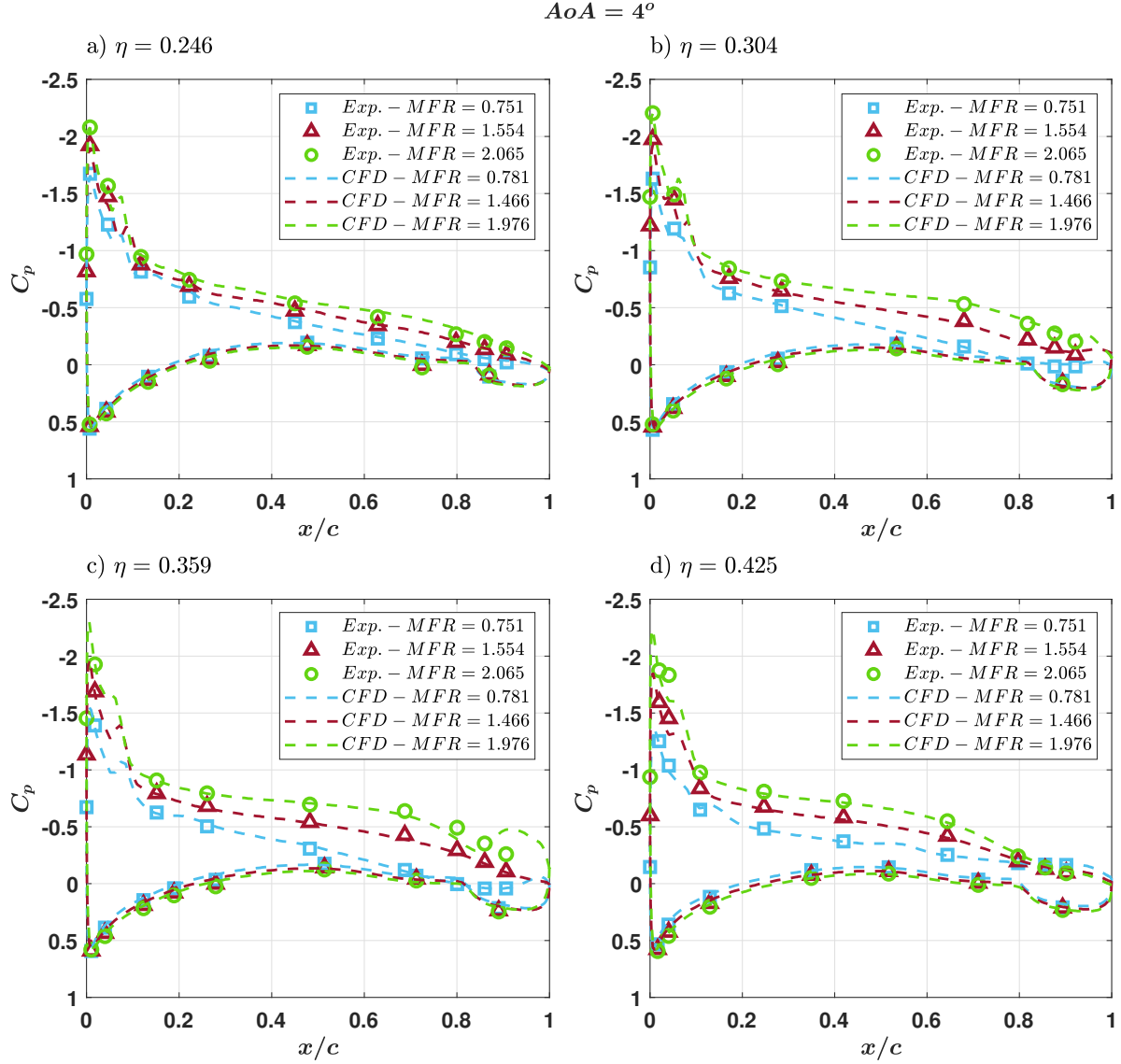


**Fig. 11** Pressure distributions for  $AoA = 4^\circ$ . The experimental results are compared with CFD data for similar MFRs.

increasing the lift. The pressure distributions obtained from CFD and the pressure taps could clearly capture this phenomenon. Moreover, it has been observed that the static pressure distributions are significantly influenced by the engine power setting for all four spanwise sections where the measurements were carried out. As expected, the MFR impact on the pressure distributions has shown to be the strongest for the sections closer to the nacelle.

- Overall, a good agreement between the numerical and experimental results was obtained both for  $C_l$ ,  $F_{net}$ , and the pressure distributions. Nonetheless, particularly for the latter, a considerable mismatch could be observed at the outboard spanwise section, especially for low  $AoAs$  and high MFRs.

This study assumed that the powered lift effect would mainly be impacted by the engine MFR and that the Reynolds dependency would be small or negligible. This assumption remains to be confirmed. Future work should assess whether or not the observed linear relation between MFR and  $C_l$  will be maintained at higher  $Re$ , representative of real low-speed flight conditions for transonic aircraft.

$$AoA = 6^\circ$$

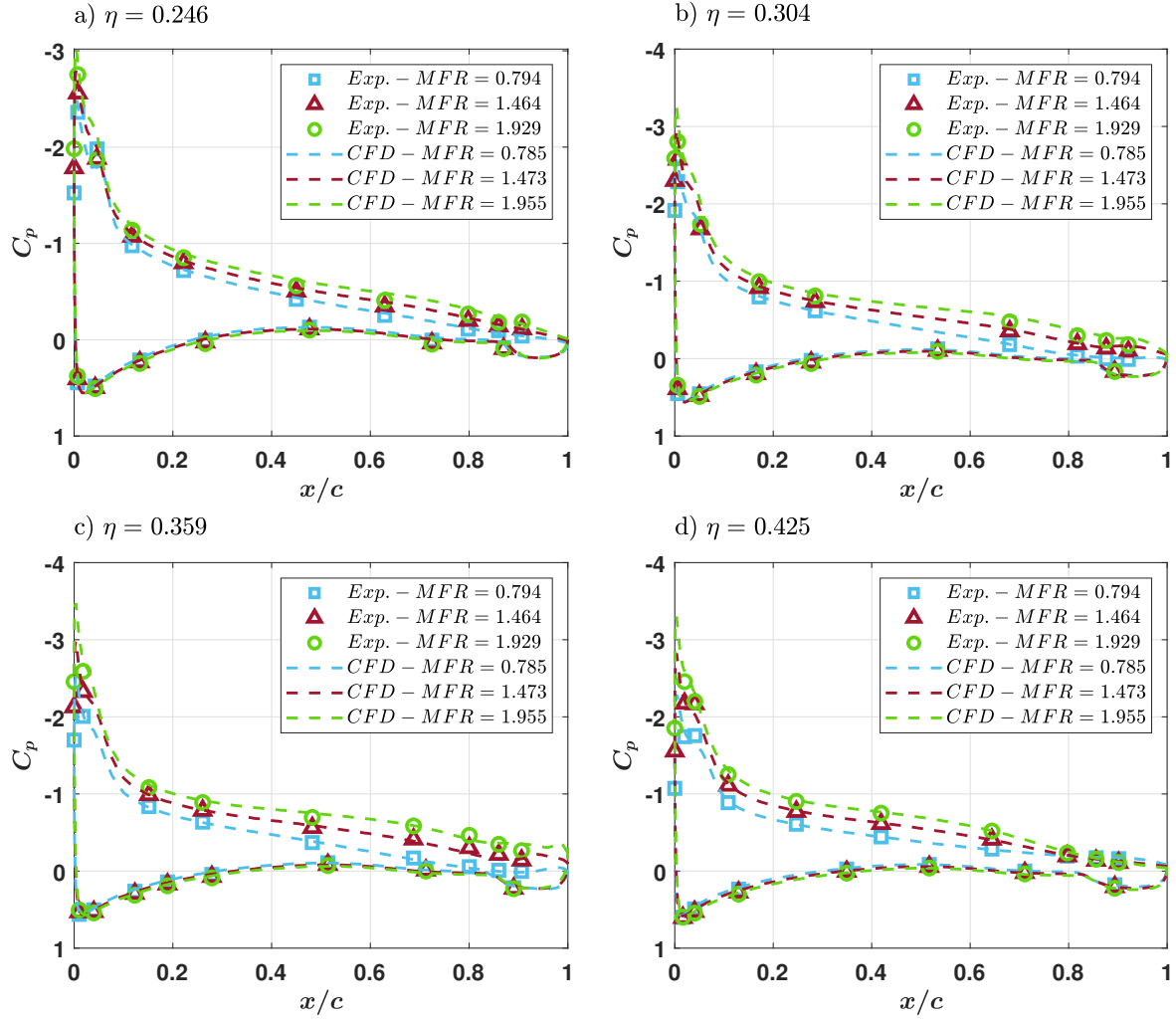


**Fig. 12** Pressure distributions for  $AoA = 6^\circ$ . The experimental results are compared with CFD data for similar MFRs.

### Acknowledgments

This research work was funded by the Swedish National Aviation Engineering Research Program, NFFP, supported by Swedish Armed Forces, the Swedish Defense Materiel Administration, Swedish Governmental Agency for Innovation Systems (VINNOVA), and GKN Aerospace. All the computations were performed using Chalmers Center for Computational Science and Engineering (C3SE) resources, provided by Swedish National Infrastructure for Computing (SNIC).

The authors would also like to thank Professor Valery Chernoray for the continuous support in the Chalmers Laboratory of Fluids and Thermal Sciences.

### References

- [1] Reshotko, M., Goodykoontz, J. H., and Dorsch, R. G., "Engine-over-the-wing Noise Research," *Journal of Aircraft*, Vol. 11, No. 4, 1974, pp. 195–196.
- [2] Guo, Y., Burley, C. L., and Thomas, R. H., "On noise Assessment for Blended Wing Body Aircraft," *52nd Aerospace Sciences Meeting*, 2014, p. 0365.

- [3] Doty, M. J., Brooks, T. F., Burley, C. L., Bahr, C. J., and Pope, D. S., "Jet Noise Shielding Provided by a Hybrid Wing Body Aircraft," *20th AIAA/CEAS aeroacoustics conference*, 2014, p. 2625.
- [4] Wick, A. T., Hooker, J. R., Clark, C. M., Plumley, R., and Zeune, C., "Powered Low Speed Testing of the Hybrid Wing Body," *55th AIAA Aerospace Sciences Meeting*, 2017, p. 0100. <https://doi.org/10.2514/6.2017-0100>.
- [5] Raymer, D., *Aircraft design: a conceptual approach*, American Institute of Aeronautics and Astronautics, Inc., 2012.
- [6] Kinney, D., Hahn, A., Gelhausen, P., Kinney, D., Hahn, A., and Gelhausen, P., "Comparison of Low and High nacelle Subsonic Transport Configurations," *15th Applied Aerodynamics Conference*, 1997, p. 2318. <https://doi.org/10.2514/6.1997-2318>.
- [7] Silva, V. T., Lundbladh, A., and Xisto, C., "Aerodynamic Installation Effects of Over the wing Mounted Ultrahigh bypass Engines," *25th International Symposium on Air Breathing Engines*, ISABE Paper 2022-145, Ottawa, Canada, 2022.
- [8] Tavares Silva, V., Lundbladh, A., Xisto, C., and Grönstedt, T., "Over-wing Integration of Ultra-high Bypass Ratio Engines: A Coupled Wing Redesign and Engine Position Study," *Aerospace Science and Technology*, 2023, p. 108350. <https://doi.org/10.1016/j.ast.2023.108350>.
- [9] Wegener, P., and Lange, F., "Integration of Wing-Mounted Over-Wing Engines on a Mid-Range Aircraft," *AIAA SCITECH 2022 Forum*, 2022, p. 2563. <https://doi.org/10.2514/6.2022-2563>.
- [10] Wegener, P., "Integration of Fuselage-mounted Over-wing Engines on a Mid-range Aircraft," *ICAS, Shanghai*, 2021.
- [11] Ahuja, J., Ashwin Renganathan, S., and Mavris, D. N., "Sensitivity Analysis of the Overwing Nacelle Design Space," *Journal of Aircraft*, Vol. 59, No. 6, 2022, pp. 1478–1492. <https://doi.org/10.2514/1.C036687>.
- [12] Hooker, J. R., Wick, A., Zeune, C. H., and Agelastos, A., "Over Wing Nacelle Installations for Improved Energy Efficiency," *31st AIAA Applied Aerodynamics Conference*, 2013, p. 2920. <https://doi.org/10.2514/6.2013-2920>.
- [13] Hooker, J. R., "Design of a Hybrid Wing Body for Fuel Efficient Air Mobility Operations at Transonic Flight Conditions," *52nd Aerospace Sciences Meeting*, 2014, p. 1285. <https://doi.org/10.2514/6.2014-1285>.
- [14] Campbell, J. P., "Overview of Powered-lift Technology," *NASA. Langley Res. Center Powered-Lift Aerodyn. and Acoustics*, 1976.
- [15] Englar, R., Gaeta, R., Lee, W., and Leone, V., "Development of Pneumatic Over-the-Wing Powered-Lift Technology. Part I: Aero/Propulsive," *27th AIAA Applied Aerodynamics Conference*, 2009, p. 3942. <https://doi.org/10.2514/6.2009-3942>.
- [16] Gaeta, R., Englar, R., and Avera, M., "Development of Pneumatic Over-the-Wing Powered-Lift Technology Part II: Aeroacoustics," *27th AIAA Applied Aerodynamics Conference*, 2009, p. 3941. <https://doi.org/10.2514/6.2009-3941>.
- [17] Chan, D. T., Hooker, J. R., Wick, A. T., Plumley, R., Zeune, C., Ol, M. V., and DeMoss, J. A., "Transonic Semispan Aerodynamic Testing of the Hybrid Wing Body With Over Wing Nacelles in the National Transonic Facility," *55th AIAA Aerospace Sciences Meeting*, 2017, p. 0098. <https://doi.org/10.2514/6.2017-0098>.
- [18] Robles, G. R., and Catalano, F. M., "The Effects of an Over-The-Wing Nacelle in the Aerodynamic Characteristics of a Conventional Aircraft," *22nd International Congress of Mechanical Engineering (COBEM 2013) November*, 2013, pp. 3–7.
- [19] de Vries, R., van Arnhem, N., Avallone, F., Ragni, D., Vos, R., Eitelberg, G., and Veldhuis, L. L. M., "Experimental Investigation of Over-the-Wing Propeller–Boundary-Layer Interaction," *AIAA Journal*, Vol. 59, No. 6, 2021, pp. 2169–2182. <https://doi.org/10.2514/1.J059770>.
- [20] Vassberg, J., Dehaan, M., Rivers, M., and Wahls, R., "Development of a Common Research Model for Applied CFD Validation Studies," *26th AIAA applied aerodynamics conference*, 2008, p. 6919. <https://doi.org/10.2514/6.2008-6919>.
- [21] Rivers, M., and Dittberner, A., "Experimental Investigations of the NASA Common Research Model in the NASA Langley National Transonic Facility and NASA Ames 11-Ft Transonic Wind Tunnel (Invited)," *49th AIAA aerospace sciences meeting including the new horizons forum and aerospace exposition*, 2011, p. 1126. <https://doi.org/10.2514/6.2011-1126>.
- [22] Silva, V. T., Lundbladh, A., Petit, O., and Xisto, C., "Multipoint Aerodynamic Design of Ultrashort Nacelles for Ultrahigh-Bypass-Ratio Engines," *Journal of Propulsion and Power*, Vol. 38, No. 4, 2022, pp. 541–558. <https://doi.org/10.2514/1.B38497>.
- [23] International Organization for Standardization, I., "General Requirements for the Competence of Testing and Calibration Laboratories, 17025," Tech. rep., International Organization for Standardization, 2008.

- [24] ASME International, A., "Test Uncertainty 19.1 - 2018," Tech. rep., ASME International ASME, 2004.
- [25] Jonsson, I., "Experimental Aerothermal Study of Internal Jet Engine Structures," Ph.D. thesis, Chalmers Tekniska Hogskola (Sweden), 2021.
- [26] Perez, B. M. R., "Aerothermal Experimental Investigation of LPT-OGVs," Ph.D. thesis, Chalmers Tekniska Hogskola (Sweden), 2017.
- [27] Pointwise, "Pointwise User Manual," Pointwise, Inc, Canonsburg, Pa, 2021.